

SIMULATION OF FLOW UNSTEADINESS IN CHEMICAL OXYGEN-IODINE LASER DEVICES

Timothy J. Madden

8 July 2005

Final Report

APPROVED FOR PUBLIC RELEASE; DISTRIBUTION IS UNLIMITED.



**AIR FORCE RESEARCH LABORATORY
Directed Energy Directorate
3550 Aberdeen Ave SE
AIR FORCE MATERIEL COMMAND
KIRTLAND AIR FORCE BASE, NM 87117-5776**

STINFO COPY

AFRL-DE-PS-TR-2005-1120

Using Government drawings, specifications, or other data included in this document for any purpose other than Government procurement does not in any way obligate the U.S. Government. The fact that the Government formulated or supplied the drawings, specifications, or other data, does not license the holder or any other person or corporation; or convey any rights or permission to manufacture, use, or sell any patented invention that may relate to them.

This report has been reviewed by the Public Affairs Office and is releasable to the National Technical Information Service (NTIS). At NTIS, it will be available to the general public, including foreign nationals.

If you change your address, wish to be removed from this mailing list, or your organization no longer employs the addressee, please notify AFRL/DELC, 3550 Aberdeen Ave SE, Kirtland AFB, NM 87117 5776.

Do not return copies of this report unless contractual obligations or notice on a specific document requires its return.

This report has been approved for publication.

//signed//

TIMOTHY J. MADDEN, DR-II,
Project Manager, AFRL/DELC

//signed//

KIP R. KENDRICK, DR-III,
Chief, AFRL/DELC

//signed//

L. BRUCE SIMPSON, SES
Director, Directed Energy Directorate

REPORT DOCUMENTATION PAGE			Form Approved OMB No. 0704-0188		
<small>Public reporting burden for this collection of information is estimated to average 1 hour per response, including the time for reviewing instructions, searching existing data sources, gathering and maintaining the data needed, and completing and reviewing this collection of information. Send comments regarding this burden estimate or any other aspect of this collection of information, including suggestions for reducing this burden to Department of Defense, Washington Headquarters Services, Directorate for Information Operations and Reports (0704-0188), 1215 Jefferson Davis Highway, Suite 1204, Arlington, VA 22202-4302. Respondents should be aware that notwithstanding any other provision of law, no person shall be subject to any penalty for failing to comply with a collection of information if it does not display a currently valid OMB control number. PLEASE DO NOT RETURN YOUR FORM TO THE ABOVE ADDRESS.</small>					
1. REPORT DATE (DD-MM-YYYY) 08-07-2005		2. REPORT TYPE Final Report		3. DATES COVERED (From - To) 05-06-2004 – 19-02-2005	
4. TITLE AND SUBTITLE Simulation of Flow Unsteadiness in Chemical Oxygen-Iodine Laser Devices			5a. CONTRACT NUMBER In-House (DF297239)		
			5b. GRANT NUMBER		
			5c. PROGRAM ELEMENT NUMBER 65502C		
6. AUTHOR(S) Timothy J. Madden			5d. PROJECT NUMBER 4866		
			5e. TASK NUMBER LB		
			5f. WORK UNIT NUMBER 08		
7. PERFORMING ORGANIZATION NAME(S) AND ADDRESS(ES) Air Force Research Laboratory/DELC 3550 Aberdeen Avenue SE Kirtland AFB, NM 87117-5776			8. PERFORMING ORGANIZATION REPORT NUMBER		
9. SPONSORING / MONITORING AGENCY NAME(S) AND ADDRESS(ES) Air Force Research Laboratory 3550 Aberdeen Avenue SE Kirtland AFB, NM 87117-5776			10. SPONSOR/MONITOR'S ACRONYM(S)		
			11. SPONSOR/MONITOR'S REPORT NUMBER(S) AFRL-DE-PS-TR-2005-1120		
12. DISTRIBUTION / AVAILABILITY STATEMENT APPROVED FOR PUBLIC RELEASE; DISTRIBUTION IS UNLIMITED.					
13. SUPPLEMENTARY NOTES					
14. ABSTRACT 3-dimensional Navier-Stokes simulations of chemical oxygen-iodine laser (COIL) hardware are performed to elucidate the unsteady fluid dynamic aspects of these flowfields. Reacting (COIL) and non-reacting flow simulations are performed on varying resolution grids to explore the unsteadiness, and comparisons to experimental data are made.					
15. SUBJECT TERMS Chemical laser, COIL, CFD, unsteady flowfield analysis, jet-in-crossflow, reacting flow simulation.					
16. SECURITY CLASSIFICATION OF:			17. LIMITATION OF ABSTRACT SAR	18. NUMBER OF PAGES 32	19a. NAME OF RESPONSIBLE PERSON Dr. Timothy J. Madden
a. REPORT UNCLASSIFIED/ UNLIMITED	b. ABSTRACT UNCLASSIFIED/ UNLIMITED	c. THIS PAGE UNCLASSIFIED/ UNLIMITED			19b. TELEPHONE NUMBER (include area code) 505.846.9076

Standard Form 298 (Rev. 8-98)
Prescribed by ANSI Std. Z39.18

This page intentionally left blank.

Table of Contents

1. Introduction	1
2. Problem and Methodology	1
3. Results	4
4. Summary and Conclusions	7
5. References	7

Figures

Figure 1. Computational grid used in the first 3-D GASP COIL simulation, utilizing a symmetry plane boundary condition at the center of the large injector orifice. The grid is shown in relation to a rendering of the wetted surfaces in the COIL laser hardware.	10
Figure 2. Computational grid used all other 3-D GASP simulations of COIL hardware, shown in relation to a rendering of the wetted surfaces in the COIL laser hardware. Note that the lateral boundaries are now between the small orifices. Also note the use of multiblock, highly orthogonal grid structure to improve grid quality over the grid used in the first simulation.	10
Figure 3. Fixed time snap shot of unsteady fluid dynamic structures manifested in the He/I ₂ jet from the first 3-D GASP COIL simulation utilizing a symmetry plane at the center of the large orifice (see Fig. 1). A surface of constant I ₂ mole fraction acts as a scalar tracer for the jet structure.	11
Figure 4. Time traces for the Z-averaged laser gain at different positions in the laser resonator section of the simulated COIL hardware. This data was taken at a sampling rate of 10 iterations of the 3-D GASP COIL simulation (see Fig. 1), for a temporal sampling rate of 1x10 ⁻⁷ sec.	11
Figure 5. Comparison of time, Z-averaged laser gain from the first unsteady COIL simulation (see Fig. 1) with experiment data and previous steady-state COIL simulations. The steady state simulations include varying levels of chemistry modeling fidelity.	12
Figure 6. Index of refraction within the 2-D plane at the center of the large injector orifice from the first 3-D GASP COIL simulation (see Fig. 1).	12
Figure 7. 3-D streamtraces (in black) initiated upstream of the large injector orifice in the first XZ plane (0.00098 cm) from the wall in conjunction with vortex cores (in red) extracted from the first 3-D GASP COIL simulation (see Fig. 1).	13
Figure 8. Lateral or Z velocity component (W) variation with time at monitoring points located along the symmetry plane in the proximity of the injector orifices from the first 3-D GASP COIL simulation (see Fig. 1).	13

Figure 9.	Streamlines, in black, vortex cores, in red, and Mach number = 1 isosurface in the jet nearfield from the He flow COIL hardware simulation (see Fig. 2). This simulation does not use the symmetry boundary at the center of the large injector orifice as in the first simulation, but uses periodic boundaries outside of the small injector orifices.	14
Figure 10.	Streamlines, in black, vortex cores, in red, and Mach number = 1 isosurface in the jet near-field from the He flow COIL hardware simulation (see Fig. 2). This simulation does not use the symmetry boundary at the center of the large injector orifice as in the first simulation, but uses periodic boundaries outside of the small injector orifices. This perspective is further removed than with Fig. 9.	14
Figure 11.	Time variance of the streamwise or X direction velocity (U) component at various monitoring points in the jet near field from the He flow COIL hardware simulation shown in Figs. 9 and 10.	15
Figure 12.	Fourier analysis of temporal variation of the streamwise or X direction velocity (U) component in Fig. 11.	15
Figure 13.	Time variance of the vertical velocity (Y) component at various monitoring points in the jet nearfield from the He flow COIL hardware simulation shown in Figs. 9 and 10.	16
Figure 14.	Fourier analysis of temporal variation of the vertical velocity (Y) component in Fig. 13.	16
Figure 15.	Time variance of the lateral velocity (Z) component at various monitoring points in the jet nearfield from the He flow COIL hardware simulation shown in Figs. 9 and 10.	17
Figure 16.	Fourier analysis of the lateral velocity (Z) component in Fig. 15.	17
Figure 17.	Time variance of the lateral velocity (Z) component at various monitoring points in the jet nearfield from the 8 million grid cell He flow COIL hardware simulation.	18
Figure 18.	Fourier analysis of the lateral velocity (Z) component in Fig. 17.	18
Figure 19.	Time variance of the streamwise or X direction velocity (U) component at various monitoring points in the jet nearfield from the He-O ₂ -I ₂ flow COIL hardware simulation.	19
Figure 20.	Fourier analysis of temporal variation of the streamwise or X direction velocity (U) component in Fig. 19.	19
Figure 21.	Time variance of the vertical or Y direction velocity (V) component at various monitoring points in the jet nearfield from the He-O ₂ -I ₂ flow COIL hardware simulation.	20
Figure 22.	Fourier analysis of temporal variation of the vertical velocity (Y) component in Fig. 21.	20
Figure 23.	Time variance of the lateral or Z direction velocity (W) component at various monitoring points in the jet nearfield from the He-O ₂ -I ₂ flow COIL hardware simulation.	21
Figure 24.	Fourier analysis of the lateral velocity (Z) component in Fig. 23.	21
Figure 25.	Time variance of the lateral or Z direction velocity (W) component at various monitoring points in the jet nearfield from the He-O ₂ -I ₂ flow COIL hardware simulation on 8 million grid cells.	22
Figure 26.	Fourier analysis of the lateral velocity (Z) component in Fig. 25.	22

Figure 27. Time variance of the lateral or Z direction velocity (W) component at various monitoring points in the jet nearfield from the COIL hardware reacting flow simulation on 1 million grid cells.	23
Figure 28. Fourier analysis of the lateral velocity (Z) component in Fig. 27.	23

Tables

Table 1. 21 reaction, 10 species COIL finite-rate chemistry mechanism used in this work.	8
Table 2. Flow rates and flow conditions used in the simulations discussed in this effort.	9

This page intentionally left blank.

1. Introduction

Theoretical models for chemical lasers depend on a variety of assumptions and empirical data to provide closure and simplify solution of the governing equations. Among the various assumptions and empirical data that have been built into models for chemical lasers are assumptions regarding flow steadiness in the time domain and geometric similarity of the spatial domain. The work discussed here is directed toward elucidating and increasing the understanding of these assumptions commonly used in chemical laser simulation and the impact of their usage upon the predictions of these models. These efforts in turn are directly linked to efforts to achieve improved chemical laser efficiency and performance, as excursions outside the assumed to be ‘well understood’ traditional operational parameter space are increasingly necessary.

2. Problem and Methodology

Madden and Miller¹ presented computational data of the chemical oxygen-iodine laser (COIL) indicating that the flowfield should be marked by substantial flow unsteadiness. Although COIL experiment data does not exist to confirm this prediction, non-reacting flow experiments at similar flow conditions performed by Fric and Roshko¹¹ do substantiate this prediction. Building on the earlier results, the objective of this work is to further elucidate the flow unsteadiness, its’ underlying physics, and the manifested effects in COIL performance.

The objective of this work is to generate understanding of the temporal and spatial dependence of the physical processes underlying chemical lasers through systematic testing of the models employed in simulation of these devices. This objective is achieved through 3-D time accurate numerical simulation of the COIL flowfield and related flowfields from similar fluid dynamic experiments.

Chemical lasers generally operate on a series of exothermic, gas phase chemical reactions that create a population inversion, or non-Boltzmann energy distribution, within the energy states of the products of reactions. As these products equilibrate towards the Boltzmann distribution of energy states, photons are emitted. If an energetically excited species A^* emits a photon of energy $h\nu$ during the equilibration process, then this photon may collide with another excited species A^* causing it to release another photon with equal energy in the same direction of propagation as the first photon. This can be described as:



As the number of photons increases, a wave builds within the gas which when directed by mirrors that transmit a fraction of the photons with each reflection of the waves becomes a laser. As the wave builds within the gas, the increase in the number of photons or the wave intensity per given unit distance leads to the concept of gain in lasers. Gain is a key performance parameter in chemical lasers and is frequently referred to in this work. COIL generates the lasing species A^* via a complex series of chemical reactions, both liquid and gas phase. The first phase occurs in liquid, and generates the ‘fuel’ via the reaction:



The electronically excited singlet-delta state of oxygen diffuses out of the liquid and is picked up by a carrier gas, usually He. COILs use collisions with ground state I atoms, $I(^2P_{3/2})$, to efficiently generate the lasing species $I^*(^2P_{1/2})$ via the collisional energy transfer process:



This reaction is more efficient at producing $I^*(^2P_{1/2})$ than any other known process, hence the reason a more direct reaction path to $I^*(^2P_{1/2})$ is not used. An additional reactive process occurs in COIL where $O_2^*(^1\Delta)$ dissociates molecular iodine, I_2 , to generate the ground state I atoms, $I(^2P_{3/2})$. This multi-step energy transfer/reactive process occurs through the following reactions:



The exact state(s) of I_2 that I_2^* represents is still somewhat of a point of contention amongst researchers at this time due to the considerable difficulty in constructing experiments to clearly identify and track multiple vibrational and electronic excited states. Because of the indeterminate nature of the I_2^* state(s) and the number of potential intermediate energy transfer processes involved, mathematical constructs are used to describe equation [4] but the construct is fitted to experimental measurements of the overall rate of dissociation of I_2 .

The gas flows within chemical lasers can best be described as the flow of particles of different chemical composition with collisional interactions occurring between the particles and between the particles and the photons within the radiation field. Mathematically, this flow of particles is treated as a continuum and is approximated by Navier-Stokes continuity equations for mass, momentum, and energy. In integral form, these equations are given by:

$$\frac{d}{dt} \iiint_{vol} \langle Q \rangle dvol + \oint_A (\vec{F} - \vec{F}_v) \cdot \hat{n} dA = \iiint_{vol} \langle S \rangle dvol \quad [5]$$

and the hyper vector of the conserved variables $\langle Q \rangle$ is:

$$\langle Q \rangle = \begin{pmatrix} \mathbf{r}_1 \\ \mathbf{M} \\ \mathbf{r}_N \\ \mathbf{r}\vec{V} \\ \mathbf{r}e_0 \end{pmatrix} = \begin{pmatrix} \mathbf{r}_1 \\ \mathbf{M} \\ \mathbf{r}_N \\ \mathbf{r}u \\ \mathbf{r}v \\ \mathbf{r}w \\ \mathbf{r}e_0 \end{pmatrix} \quad [6]$$

The inviscid flux tensor, \vec{F} , the viscous flux tensor, \vec{F}_v , and the hyper vector $\langle S \rangle$ of sources for the production and loss of the reacting species are:

$$\vec{F} = \vec{V} \langle Q \rangle + \begin{pmatrix} 0 \\ \mathbf{M} \\ 0 \\ \vec{I} \\ \vec{V} \end{pmatrix} P = \begin{pmatrix} \mathbf{r}_1 \vec{V} \\ \mathbf{M} \\ \mathbf{r}_N \vec{V} \\ \mathbf{r}\vec{V} \times \vec{V} + P\vec{I} \\ \mathbf{r}\vec{V}h_0 \end{pmatrix} \quad [7]$$

$$\vec{F}_v = \begin{pmatrix} \mathbf{r}_1 v_1 \\ \mathbf{M} \\ \mathbf{r}_N v_N \\ \vec{t} \end{pmatrix} = \begin{pmatrix} \mathbf{r}_1 v_1 \\ \mathbf{M} \\ \mathbf{r}_N v_N \\ \vec{t} \cdot \vec{V} + \vec{V} \cdot \vec{q} \end{pmatrix} \quad [8]$$

$$\langle S \rangle = \begin{pmatrix} \mathbf{R}_1 \\ \mathbf{M} \\ \mathbf{R}_N \\ 0 \\ 0 \end{pmatrix} \quad [9]$$

The production rates due to chemical reaction of the species \mathbf{r}_i are determined for each species continuity equation source by:

$$\mathbf{R}_{chemi} = m_i \sum_{j=1}^M (\mathbf{n}_{ij} - \mathbf{n}_{ji}) \left[k_{f,j} \prod_{k=1}^N \left(\frac{\mathbf{r}_k}{m_k} \right)^{\mathbf{a}_{k,j}} - k_{b,j} \prod_{k=1}^N \left(\frac{\mathbf{r}_k}{m_k} \right)^{\mathbf{a}_{k,j}} \right] \quad [10]$$

where the forward production rates of each reaction are determined from the Arrhenius rate law and the backward rates determined from the equilibrium and forward rates:

$$k_{f,j} = a_{f,j} T^{b_{f,j}} e^{\frac{e_{a,f,j}}{T}} \quad [11]$$

$$K_{eq,j} = \frac{k_{f,j}}{k_{b,j}} \quad [12]$$

$$K_{eq,j} = \left(\frac{P}{RT} \right)^{(\bar{n}_j - \bar{n}_j^0)} \exp \left(- \sum_{i=1}^N \frac{(\bar{n}_{ij} - \bar{n}_{ij}^0)}{R_i T} g_{0,i} \right) \quad [13]$$

Accurate description of molecular diffusion of chemically reacting species is important in the low pressure flowfields of chemical lasers. The Ramshaw-Dukowiczⁱⁱⁱ approximation for multi-component diffusive transport is used as opposed to higher order approximations due to the minimal loss in accuracy and lower computational cost with respect to the higher order methods. These equations, including both concentration and pressure gradient contributions are given by:

$$\begin{aligned} \dot{V}_i^r = -n_i D_{im} \left[\frac{\partial \mathbf{c}_i}{\partial r} + (\bar{c}_i - f_i) \frac{\partial \ln P}{\partial r} \right] \\ + f_i n \sum_{j=1}^N m_j D_{jm} \left[\frac{\partial \bar{c}_j}{\partial r} + (\bar{c}_j - f_j) \frac{\partial \ln P}{\partial r} \right] \end{aligned} \quad [14]$$

Finally, the key laser quantity of gain is determined from the flowfield solution using the equations:

$$a(\bar{c}_0) = \frac{7}{12} \left(\frac{A_0^2}{8p} \right) f(\bar{c}_0) \left(N_{I_2, R_{1/2}} - \frac{1}{2} N_{I_2, R_{3/2}} \right) \quad [15]$$

$$f(w(n)) = \left[\left(\frac{a^2 4 \ln 2}{p^3} \right) \frac{1}{\Delta n_D} \int_{-\infty}^{+\infty} \frac{e^{-y^2}}{(w-y)^2 + a^2} dy \right] \quad [16]$$

$$w = \frac{2 \left(\bar{n} - \bar{n}_0 \left(1 + \frac{V_z}{c} \right) \right)}{\Delta n_D} \sqrt{\ln 2} \quad [17]$$

The computational fluid dynamics (CFD) code GASP is employed to solve these equations for the simulations performed here. GASP employs domain decomposition for distribution of the computation amongst multiple processors on parallel architectures, with inner-iteration methods used to maintain fully implicit, time accurate integration of the solutions.

Reacting flow, i.e. COIL, and non-reacting flow simulations are performed in this work. The GASP COIL model utilizes 10 species mass conservation equations for the chemically reacting components of the COIL flow in addition to the base conservation equations for momentum and energy. An effective binary diffusion model is used to describe concentration and pressure contributions to mass diffusion, an important process in the low density COIL flowfield. A 10 species, 22 reaction finite-rate chemistry mechanism^{iv} is used to model the gas phase chemical kinetic processes that generate the population inversion in atomic iodine necessary for laser oscillation in COIL. This model tracks the continuity of He, O₂(¹Δ), O₂(¹Δ), O₂(¹Σ), H₂O, I₂, I₂^{*}, I^{*}P_{1/2}, I^{*}P_{3/2}, and Cl₂, a subset of the overall set of species in the flow that in conjunction with the finite-rate chemistry mechanism has been shown to accurately reproduce the COIL chemical processes. Table 1 lists these reactions and their rates.

The computational grid used for this first COIL simulation consists of 3 blocks and 3 million grid cells. The computational domain which this grid discretizes represents the smallest geometrically similar element within the COIL experiment flowfield hardware, denoted a 'unit-cell.' The unit-cell consists of a supersonic (M~2.2) converging-diverging nozzle section with one-half of a large and one small injector orifice that issue reactants into the primary flow through this nozzle. Figure 1 illustrates the unit-cell computational grid within the context of a surface rendering of the experiment's mixing nozzle. The orifices inject a sonic mixture of He and I₂ into a subsonic primary flow composed of He, O₂(¹Δ), O₂(¹Σ), H₂O, and Cl₂ with the complex 3-D flow structure associated with the jet issuing from the orifice providing the mechanism that mixes the two flows. Boundary conditions accomplish the unit-cell approximation through the enforcement of planar symmetry at the nozzle centerline in the vertical direction and at the side boundaries in the lateral direction. No-slip constant temperature boundary conditions are used at the wetted surfaces of the nozzle and orifices, with the temperature fixed at 400 K at the orifice walls and 300 K at the nozzle walls. The nozzle subsonic inflow boundary condition fixes the total pressure and total temperature and the

species fractions at constant values, while the derivative of the pressure is set to 0. The nozzle outflow boundary condition sets the second derivative of dependent variables to 0 as is appropriate for supersonic flows.

The non-reacting flow simulations follow naturally from the COIL simulation and the experiments of Eric and Roshko.ⁱⁱ These models simulate the same COIL hardware but do not split the minimum reproducible set of injector orifices with a symmetry plane. Instead, the minimum reproducible set of one large and two small injector orifices are modeled in their entirety with the lateral boundaries treated as periodic boundaries where waves exiting from one boundary enter through the opposite boundary and vice versa. The hypothesis being tested here is that the symmetry plane at the centerline of the large injector orifice interferes with the interaction of the jet wake vortices with the fluid within the jet, first developed and explored in earlier work within this line of investigation.^{iv} The computational grid used in these simulations is also somewhat different from that used in the first COIL simulation. First, the streamwise extent of the computational domain ends with the end of the isentropic expansion region of the supersonic nozzle, focusing computational effort on the injection region and transonic region of the throat. The second difference is the grid structure, with the new grid utilizing a multi-block, highly orthogonal topology that substantially increases the grid quality. Finally, this grid contains 64 million grid cells as compared to the 3 million grid cells used in the domain for the previous simulation. Fig. 2 illustrates this grid.

The boundary conditions for this simulation remain the same as those used in the first COIL simulation, with the exception of the lateral boundaries as described above to facilitate the capture of lateral fluctuations in the flow.

A sequence of physical models is tested on this grid to determine the effect of varying composition and chemical reaction upon the flowfield. The motivation for performing this test is to determine if physical models utilizing fewer species can be used to approximate the COIL fluid dynamics, and avoid the computational expense of carrying the 10 COIL species; computational costs scale approximately as the number of species squared. The models tested include a single gas He flow, a He, O₂, I₂ flow that mimics the composition of the COIL flow, and the 10 species, 22 reaction COIL model used in the first simulation. The flow conditions used as input in these simulations are shown in Table 2.

References providing additional details beyond the scope of this document may be found in Madden et al.^{vi,vii}

3. Results

We begin by reviewing and updating previous results from unsteady simulation of COIL. The 3-D GASP model for the COIL flowfield was executed in time accurate mode utilizing 1st order accurate time integration with 3rd order spatial accuracy at a physical timestep of 1.0×10^{-8} sec. The computation was advanced to a physical time of 0.001 sec, corresponding to 100,000 time steps in the computation. The physical time of 0.001 sec provides sufficient advancement of the computation to address the characteristics of the predicted flow unsteadiness.

The time accurate execution of the GASP COIL model generated a prediction of the presence of flow unsteadiness that did not decay over the 0.001 sec interval that the computation was advanced. The unsteadiness was found to extend from the jet/primary interaction region at the point of the He/I₂ transverse injection and continuing downstream undiminished. Fig. 3 illustrates the resulting impact of the flow unsteadiness upon the structure of the flow within the He/I₂ jet. Here an isosurface of 0.001 constant I mole fraction, a value approximately 1% of the concentration in the pure He/I₂, is plotted within 3-D space. The surface demonstrates the presence of regular, periodic structures associated with unsteady vortex generation, with the structures present in the flow from both the large and small orifices. Since molecular diffusion, i.e. mixing, and chemical reaction are strongly correlated with spatial gradients of reactant concentration, the presence of these unsteady flow structures is expected to have considerable impact upon this model's predictions of device performance. The evidence of this impact is shown in Fig. 4 in the laser gain, or optical wave amplification potential per unit distance, a quantity resulting directly from the COIL chemistry. Each position noted in this plot corresponds to an X, Y position with Z dependence integrally averaged to mimic the passage of photons through the media in the manner exhibited by the laser itself. The initial gain at time = 0 is from steady state conditions, and as is evident the development of the flow unsteadiness substantially changes the magnitude of the laser gain. At Positions 1 and 2 the gain decreases substantially, while at Position 3 it increases substantially. The explanation for this change is the change in the mixing characteristics and its' subsequent impact upon the progression of the chemistry. Fig. 5 shows the time, Z direction integrated average of the laser gain at various points along the X axis at the nozzle centerline in comparison with measured laser gain and that from previous steady-state simulations. In this comparison what arises is a spread of data due to the influence of advantageous and deleterious processes. Simulations using reduced chemistry mechanisms,^{vi} which underestimate the influence of performance decreasing chemical reactions, tend to align with the measured gain. When the deleterious chemical reactions are included as they are in the various full chemistry mechanisms shown, the laser gain predicted falls below the measured gain.^{vii} When the effects of flow

unsteadiness are included using the reduced chemistry mechanism, the laser gain is over-predicted with respect to the measured laser gain. A logical interpretation of this plot is that the full complexity of the COIL physics is comprised of both the full set of chemical reactions and the flow unsteadiness.

The impact of the flow unsteadiness on the optical characteristics of the COIL media is a natural concern, given the perturbations to the media caused by the flow unsteadiness. Fig. 6 shows the index of refraction, n , variation within a 2-D cut from the COIL simulation perpendicular to the direction of optical wave propagation in the device. A value of 1 represents a vacuum, where values greater than 1 occur as optical waves pass through matter. The greater the variation and the greater the value of n , the larger the phase error incurred in the optical wave as it passes through the gas. As is shown, there are local increases near the shock waves in the supersonic region of the nozzle. However, the values of n remain very close to 1, with typical values in the 5 to 10 cm region, where the laser optical resonator resides, differing from 1 by only 1 to 2×10^{-6} , a very small difference. This is due to both the very low density of the gas, and the dominant composition of He which has a very low index of refraction relative to a vacuum.

The work of Fric and Roshko indicated that a variety of structures in the jet-in-crossflow were associated with the presence of flow unsteadiness. Among these are 'wake vortices' that project from the wall boundary layer behind the jet. Three-dimensional perspective can help to further elucidate the wake structure prediction by the simulation. To elucidate the flow structure, 3-D stream traces are initiated upstream of the large injector orifice in the XZ plane adjacent to the wall, as shown in Fig. 7. In addition to the stream traces, vortex cores in this region of the computational domain are extracted and plotted in Fig. 7 using the vortex core identification functions of Sujudi and Haimes^{viii} as implemented in the CFD Analyzer software from Amtec Engineering. While vortex cores are captured and streamlines are shown projecting downward from the wall toward the backside of the jet, no vortex cores are associated with this downward projecting fluid, indicating lack of rotation. Additionally, this downward projecting fluid is adjacent to the symmetry plane at the centerline of the large injector orifice, suggesting that the symmetry plane may interfere with the development of the 'wake' vortex structures. The absence of these structures suggests that the flow physics are not completely captured in this simulation, and that the captured characteristics of the flow unsteadiness in the simulation may not be correct. Fig. 8 supports this notion, plotting the velocity component normal to the symmetry plane at a variety of monitoring points around the jet at the first cell center off of this boundary. As can be seen, these velocities at between 0 and 3 m/sec are negligible in comparison to the primary streamwise velocity component at order 200 m/sec and the jet velocity of order 1000 m/sec.

The second simulation tests the hypothesis regarding the interference of the symmetry plane at the midplane of the large injector orifice by removing this boundary and placing periodic boundaries at the plane midway between the small injector orifices, thus encompassing the whole large injector orifice and both small injector orifices. Also, the flow is composed of the COIL diluent gas He alone to reduce the computational cost for this test that is for examination of the fluid dynamic aspects of the COIL flow.

The GASP model for this simulation was executed using 1st order temporal and 3rd order spatial accuracy. The physical timestep used was 1.0×10^{-8} sec for 55,000 timesteps, advancing the flow in time to 0.00055 sec. The flow features captured by this simulation are shown in different perspectives in Figs. 9 and 10. Figs. 9 and 10 show a composite of streamtraces initiated in the boundary layer upstream of the large injector orifice, vortex cores, and a Mach number = 1 isosurface in the nearfield of the orifices. The streamlines trace the primary boundary layer flow as it passes around the large injector jet and wraps around it. As the streamlines wrap around the back side of the large injector jet, they project downward with rotation in a manner consistent the wake vortex structures observed by Fric and Roshko. Vortex cores are extracted at the center of these structures, confirming their interpretation as wake vortices. Comparing with this same plot for the reacting COIL simulation in Fig. 7 where vortex cores were not found in conjunction with the downward projecting streamlines, the conclusion to be drawn is that the symmetry boundary condition at the centerline plane of the large injector orifice interfered with the formation of the wake vortices. Fig. 10 shows the same perspective in Fig. 9 from a greater distance to provide greater detail regarding the interaction between the wake vortices and the fluid from the injector orifices. As the wake vortices project downward, they impact the back side of the fluid from the injector orifice and change trajectory to follow that of the fluid from the orifices. This behavior is noted not just with the interaction of the wake vortices behind the large injector orifice with its' fluid, but also with those behind the small injector orifices and the small injector jet. Examining the Mach number = 1 isosurface in Figs. 9 and 10 shows that one set of characteristic vortices identified by Fric and Roshko in their experiments, the 'ring' vortices that initiate on the upstream side of the jet in the region where the primary and secondary flow boundary layer interact and wrap circumferentially about the jet, are absent from this flow. The absence of these structures may indicate a fundamental difference between the strongly compressible COIL flowfield and the low Mach number, incompressible flowfield in the Fric and Roshko experiment, with the shocks present in the COIL jet structure inhibiting the formation of these 'ring' vortices.

An analysis of the fluctuations associated with the interaction between the wake vortices and the jet is shown in Figs. 11 - 16 plotting the temporal variation of the flow velocity components and Fourier analysis of these variations. These plots show that of the 10 monitoring points located in the proximity of the jet, Points 3 and 4 demonstrate the largest amplitude fluctuations. Both of these points are located on the backside of the large injector orifice jet where the interactions with the wake vortices occur. As can be seen, the fluctuations occur with all 3 velocity components. Of special note is the fluctuation in the Z direction that is perpendicular to the symmetry plane of the large injector orifice. The large amplitude of this fluctuation, a factor of 10 greater than those in Fig. 8 from the COIL simulation where the symmetry boundary is present, confirms the expectation that removal of the symmetry boundary condition at the centerline plane of the large injector orifice would facilitate its capture in the simulation.

Fourier analysis of these fluctuations indicates dominant frequencies of 74.8 kHz and 147.4 kHz in the U and V velocity components for Points 3 and 4 on the downstream side of the large injector orifice jet; Points 6 - 9 near the wall behind the small injector orifice jets have dominant frequencies at 37.4 and 74.8 kHz in the U and V velocity components. The remaining points follow the frequency distribution of Points 3 and 4. The W or lateral velocity component of particular interest here has dominant frequencies of 37.4, 110.0, and 184.8 kHz. Points 6-9 have these same dominant frequencies plus dominant frequencies at 74.8 and 147.4 kHz. The behavior suggests that the frequencies associated with the large injector orifice jet dominate the flowfield, but the small jet orifices have their own frequencies superimposed upon the wave pattern generated by the large jet. Since diameter of the small injector orifice is exactly $\frac{1}{2}$ of the diameter of the large injector orifice, one would expect resonances at the frequencies of the large jet and self resonances at frequencies differing by a factor of 2.

A separate execution of this same model using the same execution configuration was performed using factor of 2 decreases in the number of grid cells in each spatial direction, giving a total of 8 million grid cells as opposed to 64 million grid cells in the previous simulation. This allows estimates for sensitivity of the calculation to grid density to be performed. Figs. 17, 18 show the temporal variation of the W velocity component and the Fourier analysis of this data. Comparing the amplitude of the fluctuations at Points 3 and 4 to the dense grid, we see amplitudes of 18.5 and 22.5 m/sec respectively in this grid versus 21.2 and 27.0 m/sec in the dense grid. The dominant frequencies at Points 3 and 4 are 36.0, 108.4, and 180.4 kHz versus 37.4, 110.0, and 184.8 kHz on the 64 million cell grid. The better frequency resolution on the smaller grid afforded by the longer physical time advancement, 0.0021 sec versus 0.0005 sec on the 64 million cell grid did not substantially change the frequency response of the flow, nor did the differences in spatial resolution. With regard to fluctuation amplitude differences between the grids, increased numerical dissipation on the 8 million cell grid may account for some or all of the differences. However, it is also possible that small shifts in the locations of various fluid dynamic structures underlying the unsteadiness occur when going from one grid to the other, changing the response characteristics at the monitoring points that are located at the same positions for both simulations. It should be noted that this same behavior of increasing fluctuation amplitude with decreasing grid resolution while maintaining similar fluctuation frequency was observed previously by Madden and Miller¹ for 2-D simulations of the cylinder-in-crossflow.

To test the effect of flow composition, a simulation using He, O₂, and I₂ to mimic the COIL composition was executed using the same execution parameters from the previous simulations with advancement to 0.00013 sec. Figs. 19 - 24 show the velocity component temporal variation and Fourier analysis using the 64 million grid cell grid. The primary fluctuation frequencies in the U velocity component occur at 61.5, 192.3, and 330.8 kHz; 38.5, 61.5, 84.6, 184.6, 338.5 kHz for the V velocity component; and 169.2 kHz for the W velocity component with Points 3 and 4 dominating the fluctuation energy. The lower frequencies in the range of 10 to 50 kHz are not well developed and will be resolved by advancing the simulation further in time. As can be seen in the temporal variation plots, the amplitude of the fluctuations is attenuated somewhat in time, although temporal advancement is not sufficient to determine whether the amplitudes will further diminish or level-off with time.

Comparing the He-O₂-I₂ flow simulation with the He flow simulation, the 100 to 300 kHz frequency range contains the highest energy as opposed to the 30 to 80 kHz range in the He simulation, although high amplitude components do exist at 110 and 184.8 kHz in the He case. Simulation of the He-O₂-I₂ flow on the 8 million cell grid provides another point of comparison, particularly with resolution of frequencies into the 100 Hz range as shown for the W velocity component in Figs. 25, 26. As indicated, the most energetic frequencies captured on the 8 million cell grid occur at 22.0 and 162.4 kHz with the higher frequency dominating in energy by a factor of 10, similar to the 64 million cell simulation. Thus He flow simulation tends to favor the lower frequency range, whereas the He-O₂-I₂ flow simulation tends to strongly favor the high frequency, attributable to differences in the freestream velocity upstream of the jets which is 374 m/sec in the He flow and 221 m/sec in the He-O₂-I₂ flow.

Similar to the comparison of the results on the 8 million and 64 million grid cell simulations for the He flow, the He-O₂-I₂ flow simulation shows greater differences in fluctuation amplitude than in frequency. Comparing the W velocity fluctuations at Point 4 shows the amplitude near the end of the physical time advancement to be 63.5 m/sec

on the 64 million cell grid as opposed to 98.5 m/sec on the 8 million cell grid; amplitudes at Point 3 were negligibly small for this flow. Again, the effect of grid resolution on fluctuation amplitude is found to be pronounced.

Finally, initial results for a full reacting flow COIL simulation utilizing a 1 million grid cell version of the 64 and 8 million cell grids discussed above are shown in Figs. 27, 28. Given the observations regarding the effect of decreasing grid resolution on fluctuation amplitude, the important result is the observed fluctuation frequency. The peak fluctuation frequency observed in this simulation within the limits of the advancement in physical time is 113.6 kHz, consistent with the higher frequency fluctuations found in the He-O₂-I₂ flow simulation.

The attention paid to this detail, while seemingly trivial on the surface, is justified based upon the impact that these fluctuations have upon COIL performance. As demonstrated earlier, the fluctuations have a significant impact upon the laser gain through the mixing and chemistry. An additional impact occurs through Doppler shifts to the frequency of radiation that the atoms in the resonator field experience due to the fact that they are translating with a bulk velocity, causing a decrease in laser gain, shown explicitly in equations [15]-[17]. Z direction fluctuations are significant for this particular hardware since the primary direction of transit of the radiation through the device is in the Z direction. In similar COIL hardware, fluctuations in the Y direction would be significant in this same sense because the path of optical transit is in the Y direction.

4. Summary and Conclusions

In conclusion, the results provided here establish that the unit-cell approximation as previously implemented in simulations of the COIL flowfield with a symmetry plane boundary splitting an injector orifice interferes with the capture of flow structures associated with unsteadiness. Non-reacting and reacting simulations of COIL hardware indicate that lateral passage of waves normal to this symmetry plane is associated with fluctuations in the flow about this plane. An examination of the effect of variations in flow composition from He to He-O₂-I₂ to the full COIL species set showed that the He flow tended to fluctuate predominantly in the 30 to 80 kHz range whereas the He-O₂-I₂ and COIL flows fluctuated in the 100 to 300 kHz range. In the reacting flow COIL simulation where the symmetry plane was present, the flow unsteadiness found there was shown to have a substantial effect on the laser gain prediction.

Future work will continue the line of investigation initiated with the reacting flow COIL simulation using the full unit-cell as well as larger domains incorporating adjacent injector orifices laterally and across the nozzle centerline.

5. References

- ⁱ Madden, T. J. and Miller, J. H., "Simulation of Flow Unsteadiness in Chemical Laser Flowfields," AIAA-2004-0805, 42nd AIAA Aerospace Sciences Meeting and Exhibit, Reno, NV, 5-8 Jan, 2004.
- ⁱⁱ Fric, T. F., and Roshko, A., "Vortical structure in the wake of a transverse jet," *J. Fluid Mech.*, **279** 1-47, 1994.
- ⁱⁱⁱ Ramshaw, J. D. and Dukowicz, J. K., "APACHE: A Generalized Mesh Eulerian Computer Code for Multicomponent Chemically Reactive Fluid Flow," Los Alamos Report LA-7427, Jan. 1979.
- ^{iv} Perram, G. P., *Int. J. Chem. Kinet.*, **27**, 817-28 (1995).
- ^v Madden, T. J. and Miller, J. H., "An Analysis of Mechanisms of Flow Unsteadiness in Chemical Oxygen-Iodine Laser Flowfields," AIAA-2004-2728, 35th AIAA Plasmadynamics and Lasers Conference, Portland, OR, June 28-July 1, 2004.
- ^{vi} Madden, T. J. and Solomon, W. C., AIAA 97-2387, 28th Plasmadynamics and Lasers Conference, Atlanta, GA, June 23-25, 1997.
- ^{vii} Madden, T. J., SPIE Proceedings of XIV International Symposium On Gas Flow & Chemical Lasers and High Power Laser Conference, Wroclaw, Poland, 25-30 August, 2002.
- ^{viii} Sujudi, D. and Haimes, R., "Identification of Swirling Flow in 3-D Vector Fields," AIAA Paper 95-1715, San Diego CA, Jun. 1995

	Reaction	Rate (cc/molecule-sec)
1	$O_2(^1\Delta) + O_2(^1\Delta) \rightarrow O_2(^1\Sigma) + O_2(^3\Sigma)$	$2.7 \cdot 10^{-17}$
2	$O_2(^1\Sigma) + H_2O \rightarrow O_2(^3\Sigma) + H_2O$	$6.7 \cdot 10^{-12}$
3	$O_2(^1\Delta) + O_2(^3\Sigma) \rightarrow O_2(^3\Sigma) + O_2(^3\Sigma)$	$1.6 \cdot 10^{-18}$
4	$O_2(^1\Delta) + H_2O \rightarrow O_2(^3\Sigma) + H_2O$	$4.0 \cdot 10^{-18}$
5	$O_2(^1\Delta) + Cl_2 \rightarrow O_2(^3\Sigma) + Cl_2$	$6.0 \cdot 10^{-18}$
6	$O_2(^1\Delta) + He \rightarrow O_2(^3\Sigma) + He$	$8.0 \cdot 10^{-21}$
7	$I_2 + O_2(^1\Sigma) \rightarrow 2I(^2P_{3/2}) + O_2(^3\Sigma)$	$4.0 \cdot 10^{-12}$
8	$I_2 + O_2(^1\Sigma) \rightarrow I_2 + O_2(^1\Delta)$	$1.6 \cdot 10^{-11}$
9	$I_2 + O_2(^1\Delta) \rightarrow I_2^* + O_2(^3\Sigma)$	$7.0 \cdot 10^{-15}$
10	$I_2 + I(^2P_{1/2}) \rightarrow I(^2P_{3/2}) + I_2^*$	$3.8 \cdot 10^{-11}$
11	$I_2^* + O_2(^1\Delta) \rightarrow 2I(^2P_{3/2}) + O_2(^3\Sigma)$	$3.0 \cdot 10^{-10}$
12	$I_2^* + O_2(^3\Sigma) \rightarrow I_2 + O_2(^3\Sigma)$	$5.0 \cdot 10^{-11}$
13	$I_2^* + H_2O \rightarrow I_2 + H_2O$	$3.0 \cdot 10^{-10}$
14	$I_2^* + He \rightarrow I_2 + He$	$3.2 \cdot 10^{-11}$
15	$I(^2P_{3/2}) + O_2(^1\Delta) \rightarrow I(^2P_{1/2}) + O_2(^3\Sigma)$	$2.33 \cdot 10^{-8}/T$
16	$I(^2P_{1/2}) + O_2(^3\Sigma) \rightarrow I(^2P_{3/2}) + O_2(^1\Delta)$	$3.1 \cdot 10^{-8}/T \cdot \exp(-401.4/T)$
17	$I(^2P_{3/2}) + O_2(^1\Delta) \rightarrow I(^2P_{3/2}) + O_2(^3\Sigma)$	$1.0 \cdot 10^{-15}$
18	$I(^2P_{1/2}) + O_2(^1\Delta) \rightarrow I(^2P_{3/2}) + O_2(^1\Sigma)$	$1.1 \cdot 10^{-13}$
19	$I(^2P_{1/2}) + O_2(^1\Delta) \rightarrow I(^2P_{3/2}) + O_2(^3\Sigma)$	$5.0 \cdot 10^{-14}$
20	$I(^2P_{1/2}) + I(^2P_{3/2}) \rightarrow I(^2P_{3/2}) + I(^2P_{3/2})$	$1.6 \cdot 10^{-14}$
21	$I(^2P_{1/2}) + H_2O \rightarrow I(^2P_{3/2}) + H_2O$	$2.0 \cdot 10^{-12}$

Table 1. 21 reaction, 10 species COIL finite-rate chemistry mechanism used in this work.

	COIL	He-He	He-O ₂ -I ₂
Primary Flow			
T ₀ (K)	300	293	293
P ₀ (torr)	72	66.17	71.9
Utilization	0.94	0.0	0.0
Yield	0.5	0.0	0.0
Molar Flow Rate(mol/s)			
He	1.5	3.012	1.5
O ₂ (³ Σ)	0.23	0.0	0.5
O ₂ (¹ Δ)	0.23	0.0	0.0
H ₂ O	0.1	0.0	0.0
Cl ₂	0.039	0.0	0.0
Secondary Flow			
T ₀ (K)	425	327	425
P ₀ (torr)	240	56.17	240
Molar Flow Rate(mol/s)			
He	0.65	0.726	0.65
I ₂	0.0075	0.0	0.0075

Table 2. Flow rates and flow conditions used in the simulations discussed in this effort.

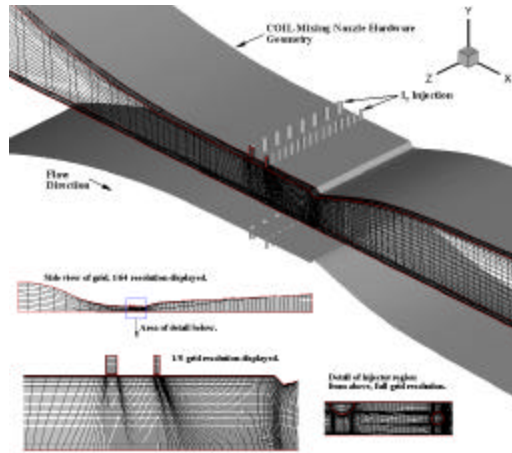


Figure 1. Computational grid used in the first 3-D GASP COIL simulation, utilizing a symmetry plane boundary condition at the center of the large injector orifice. The grid is shown in relation to a rendering of the wetted surfaces in the COIL laser hardware.

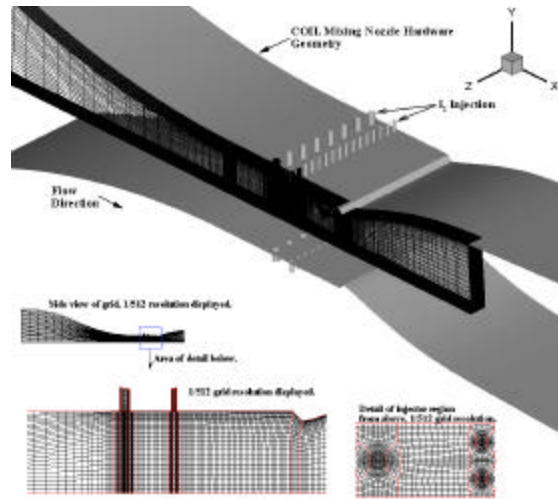


Figure 2. Computational grid used all other 3-D GASP simulations of COIL hardware, shown in relation to a rendering of the wetted surfaces in the COIL laser hardware. Note that the lateral boundaries are now between the small orifices. Also note the use of multiblock, highly orthogonal grid structure to improve grid quality over the grid used in the first simulation.

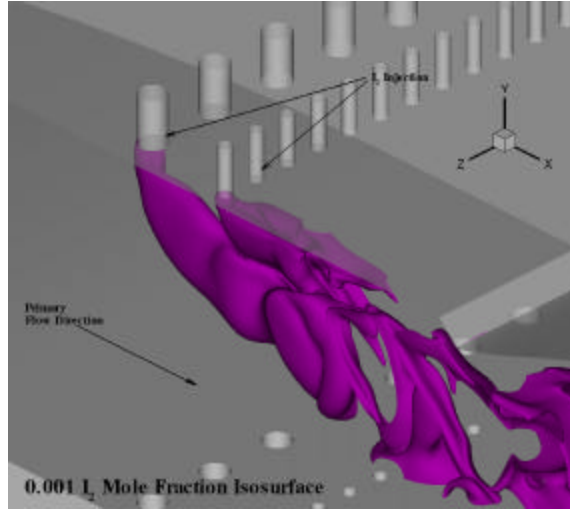


Figure 3. Fixed time snap shot of unsteady fluid dynamic structures manifested in the He/I_2 jet from the first 3-D GASP COIL simulation utilizing a symmetry plane at the center of the large orifice (see Fig. 1). A surface of constant I_2 mole fraction acts as a scalar tracer for the jet structure.

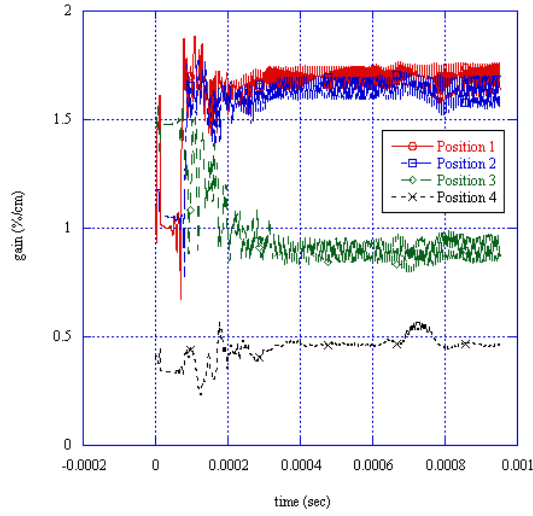


Figure 4. Time traces for the Z-averaged laser gain at different positions in the laser resonator section of the simulated COIL hardware. This data was taken at a sampling rate of 10 iterations of the 3-D GASP COIL simulation (see Fig. 1), for a temporal sampling rate of 1×10^{-7} sec.

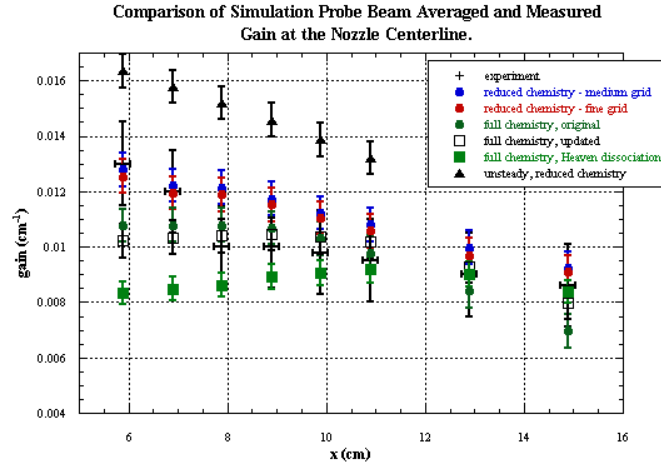


Figure 5. Comparison of time, Z-averaged laser gain from the first unsteady COIL simulation (see Fig. 1) with experiment data and previous steady-state COIL simulations.^{vii} The steady state simulations include varying levels of chemistry modeling fidelity.

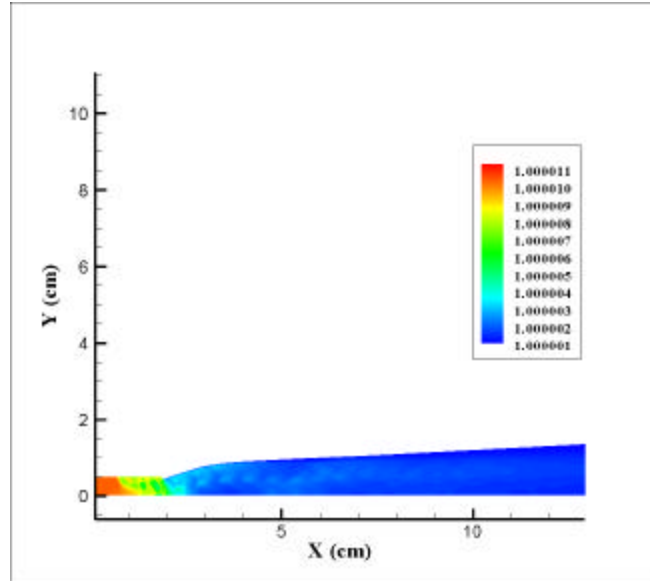


Figure 6. Index of refraction within the 2-D plane at the center of the large injector orifice from the first 3-D GASP COIL simulation (see Fig. 1).

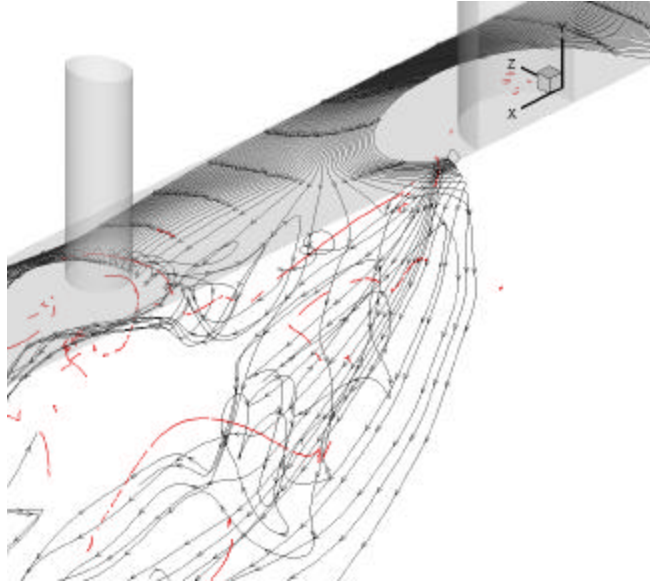


Figure 7. 3-D streamtraces (in black) initiated upstream of the large injector orifice in the first XZ plane (0.00098 cm) from the wall in conjunction with vortex cores (in red) extracted from the first 3-D GASP COIL simulation (see Fig. 1).

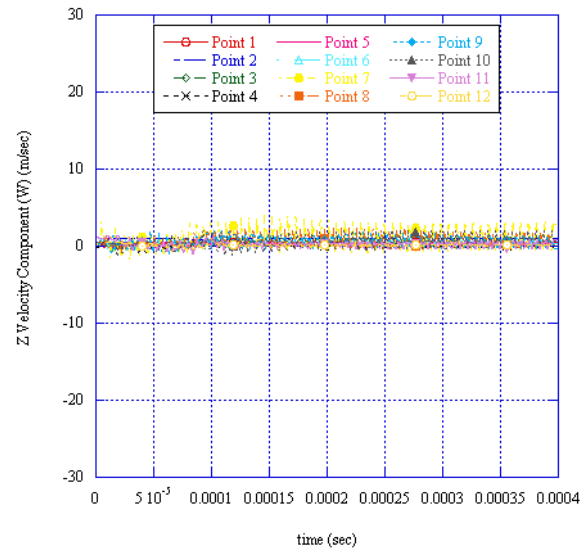


Figure 8. Lateral or Z velocity component (W) variation with time at monitoring points located along the symmetry plane in the proximity of the injector orifices from the first 3-D GASP COIL simulation (see Fig. 1).

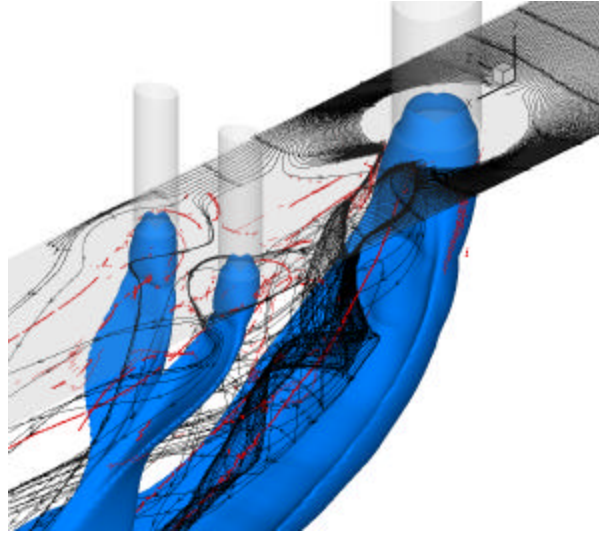


Figure 9. Streamlines, in black, vortex cores, in red, and Mach number =1 isosurface in the jet nearfield from the He flow COIL hardware simulation (see Fig. 2). This simulation does not use the symmetry boundary at the center of the large injector orifice as in the first simulation, but uses periodic boundaries outside of the small injector orifices.

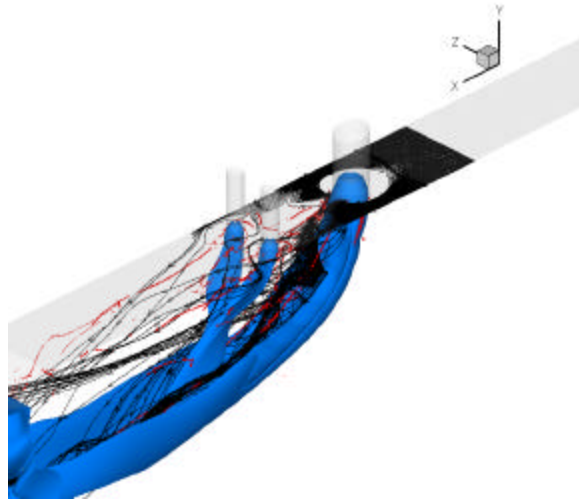


Figure 10. Streamlines, in black, vortex cores, in red, and Mach number =1 isosurface in the jet near-field from the He flow COIL hardware simulation (see Fig. 2). This simulation does not use the symmetry boundary at the center of the large injector orifice as in the first simulation, but uses periodic boundaries outside of the small injector orifices. This perspective is further removed than with Fig. 9.

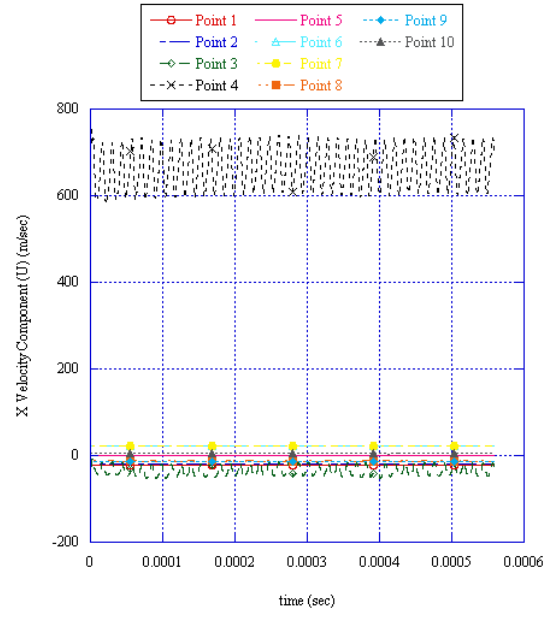


Figure 11. Time variance of the streamwise or X direction velocity (U) component at various monitoring points in the jet nearfield from the He flow COIL hardware simulation shown in Figs. 9 and 10.

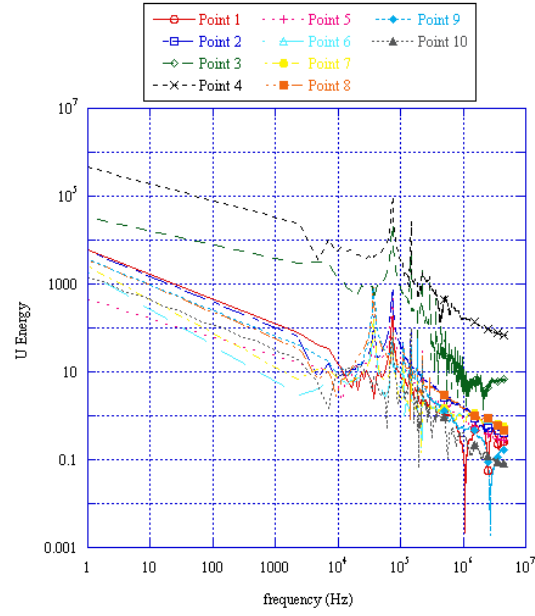


Figure 12. Fourier analysis of temporal variation of the streamwise or X direction velocity (U) component in Fig. 11.

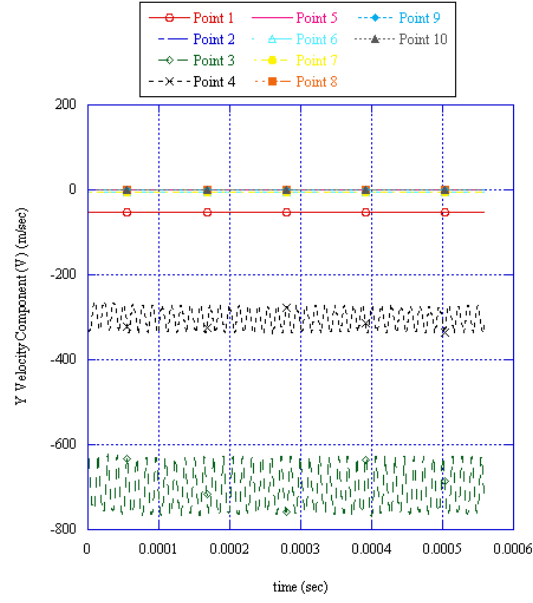


Figure 13. Time variance of the vertical velocity (Y) component at various monitoring points in the jet nearfield from the He flow COIL hardware simulation shown in Figs. 9 and 10.

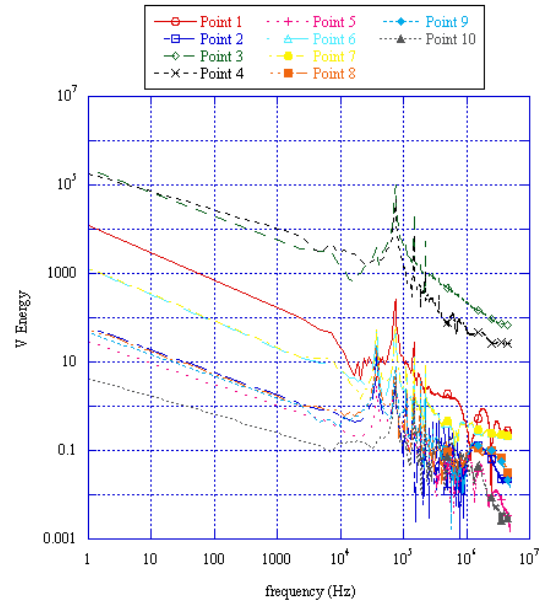


Figure 14. Fourier analysis of temporal variation of the vertical velocity (Y) component in Fig. 13.

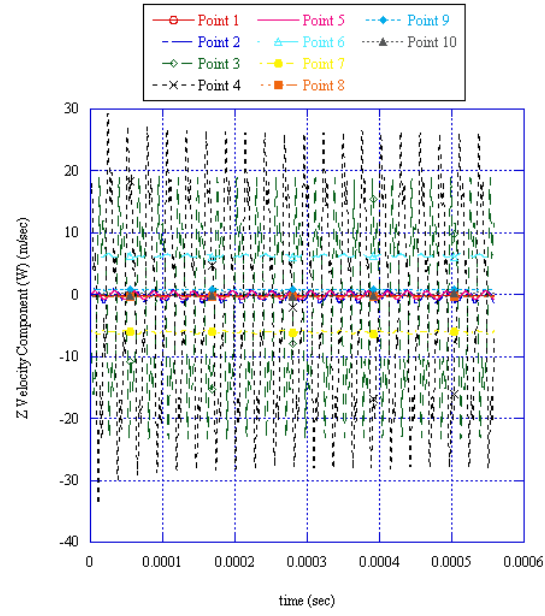


Figure 15. Time variance of the lateral velocity (Z) component at various monitoring points in the jet nearfield from the He flow COIL hardware simulation shown in Figs. 9 and 10.

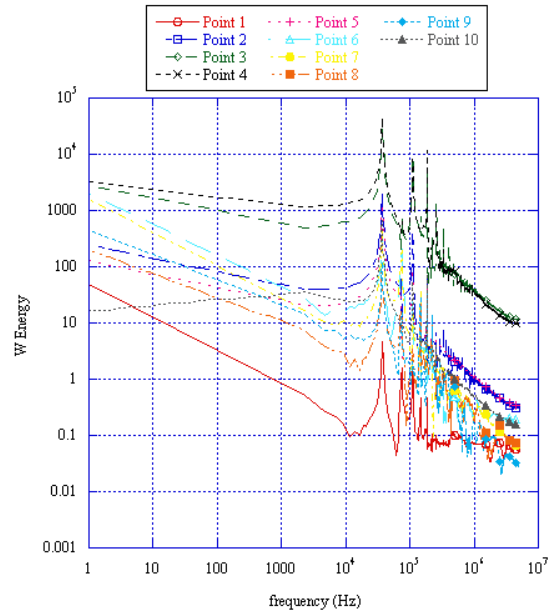


Figure 16. Fourier analysis of the lateral velocity (Z) component in Fig. 15.

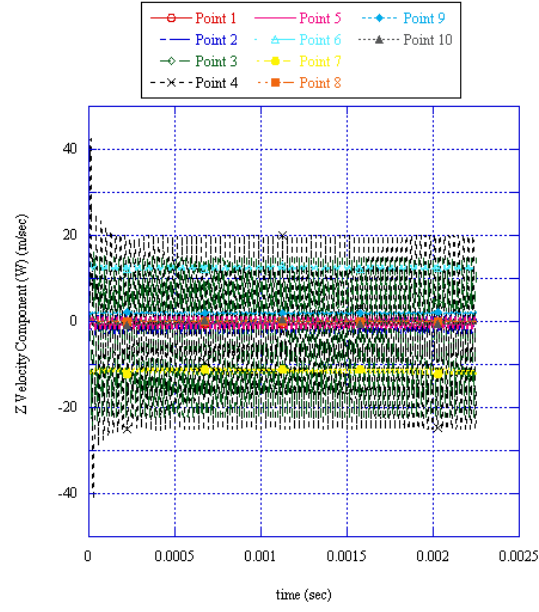


Figure 17. Time variance of the lateral velocity (Z) component at various monitoring points in the jet nearfield from the 8 million grid cell He flow COIL hardware simulation.

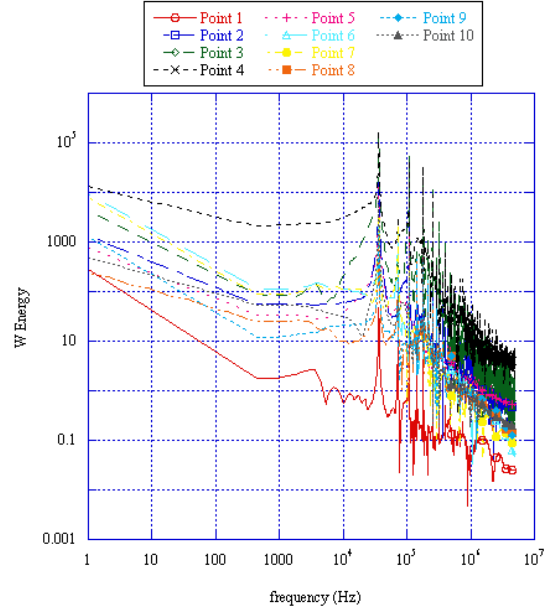


Figure 18. Fourier analysis of the lateral velocity (Z) component in Fig. 17.

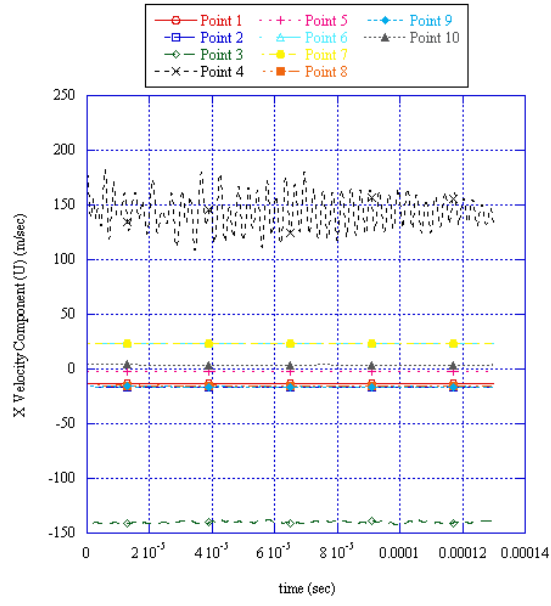


Figure 19. Time variance of the streamwise or X direction velocity (U) component at various monitoring points in the jet nearfield from the He-O₂-I₂ flow COIL hardware simulation.

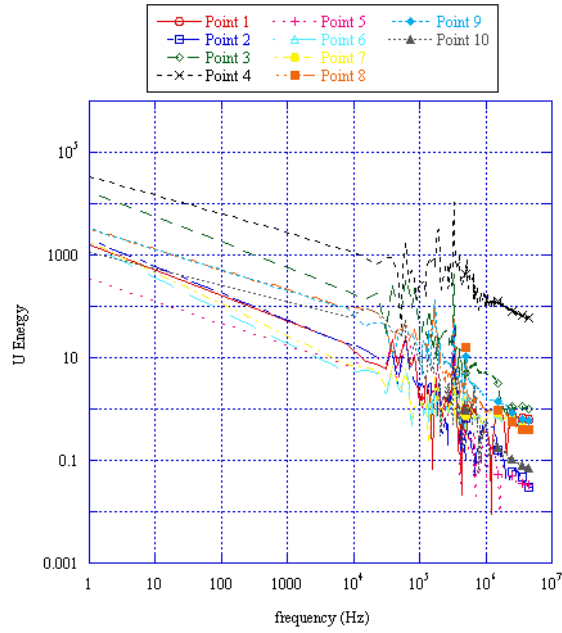


Figure 20. Fourier analysis of temporal variation of the streamwise or X direction velocity (U) component in Fig. 19.

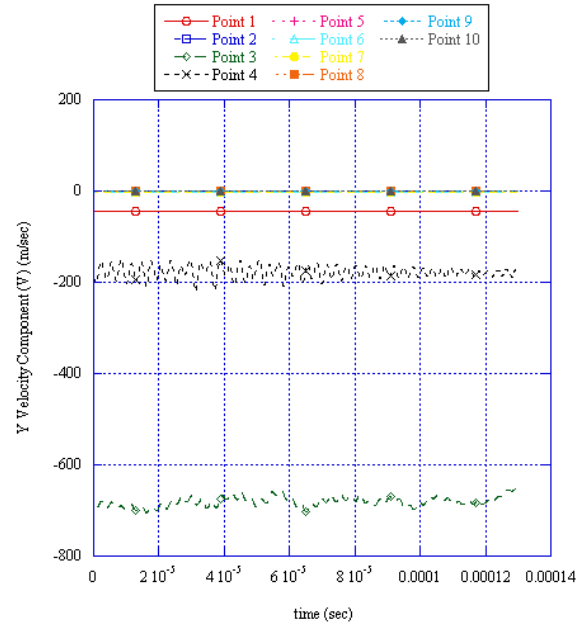


Figure 21. Time variance of the vertical or Y direction velocity (V) component at various monitoring points in the jet nearfield from the He-O₂-I₂ flow COIL hardware simulation.

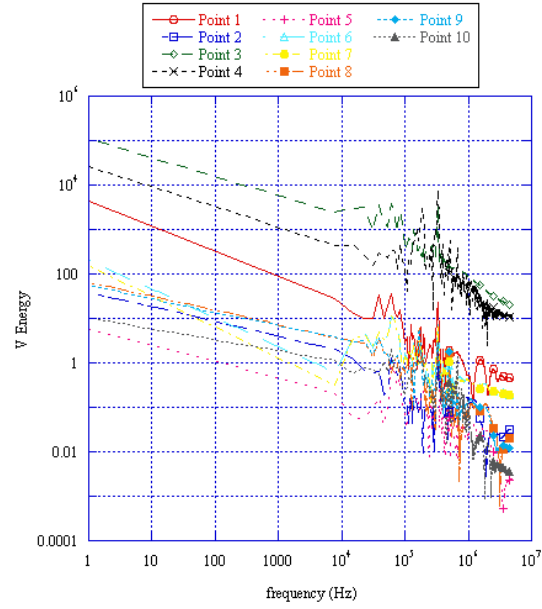


Figure 22. Fourier analysis of temporal variation of the vertical velocity (Y) component in Fig. 21.

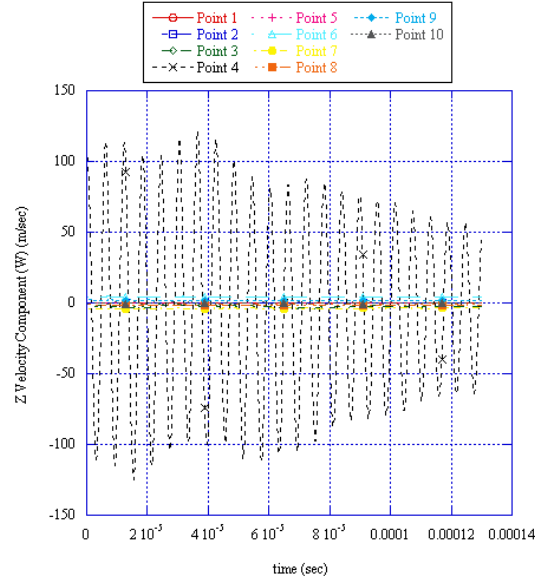


Figure 23. Time variance of the lateral or Z direction velocity (W) component at various monitoring points in the jet nearfield from the He-O₂-I₂ flow COIL hardware simulation.

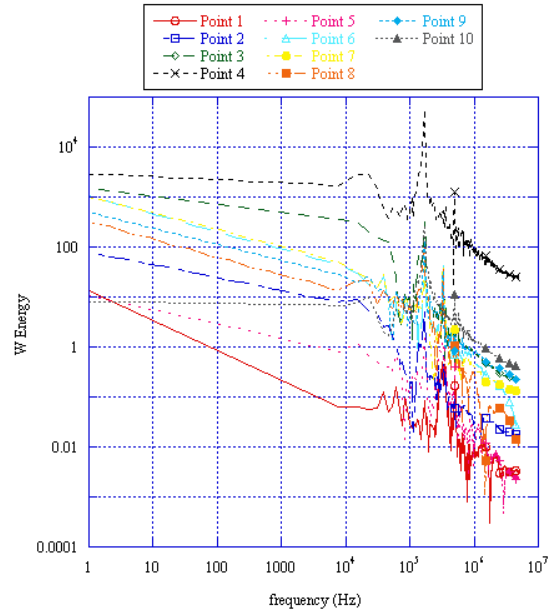


Figure 24. Fourier analysis of the lateral velocity (Z) component in Fig. 23.

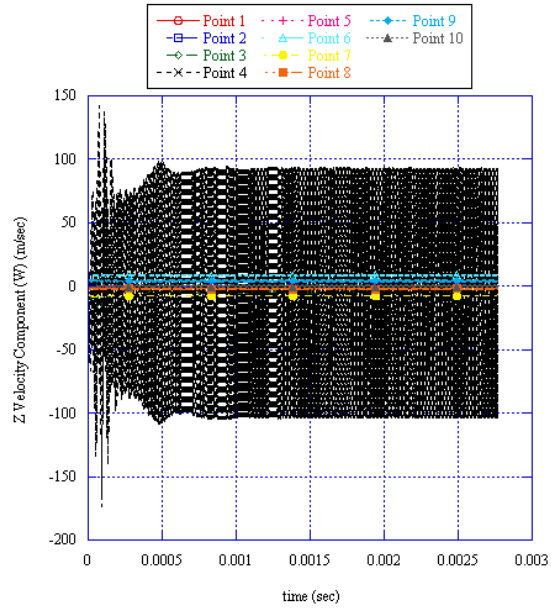


Figure 25. Time variance of the lateral or Z direction velocity (W) component at various monitoring points in the jet nearfield from the He-O₂-I₂ flow COIL hardware simulation on 8 million grid cells.

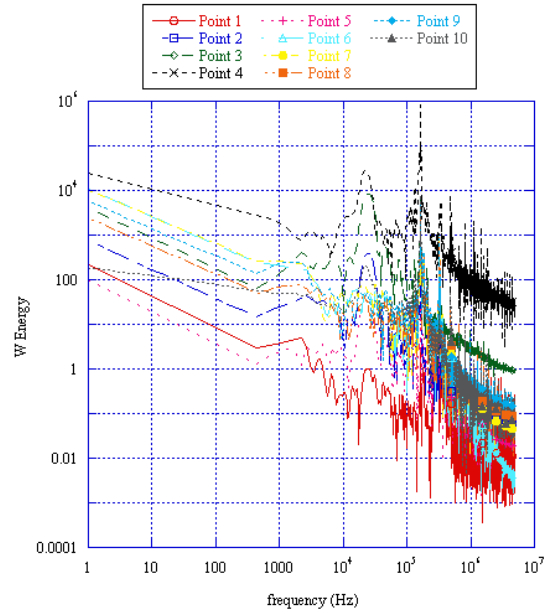


Figure 26. Fourier analysis of the lateral velocity (Z) component in Fig. 25.

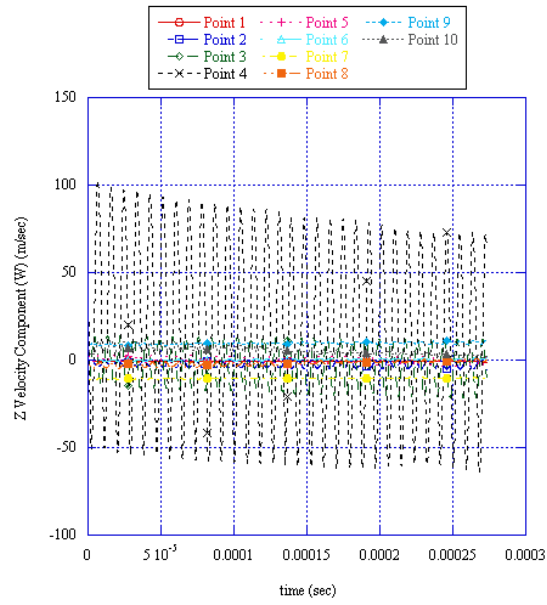


Figure 27. Time variance of the lateral or Z direction velocity (W) component at various monitoring points in the jet nearfield from the COIL hardware reacting flow simulation on 1 million grid cells.

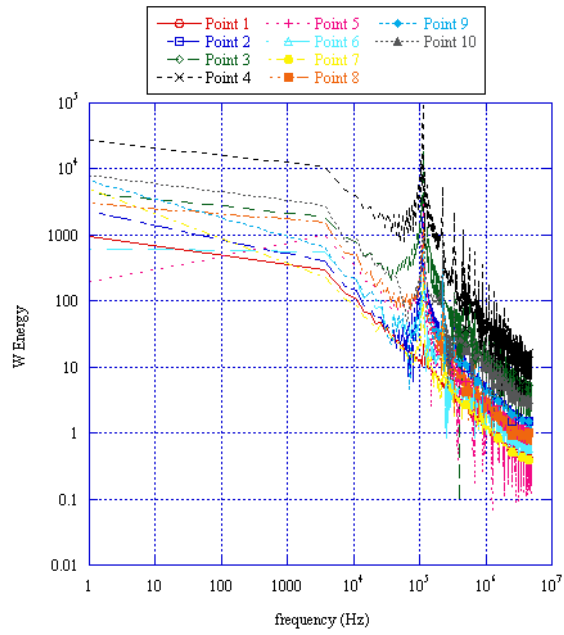


Figure 28. Fourier analysis of the lateral velocity (Z) component in Fig. 27.

DISTRIBUTION LIST

DTIC/OCP 8725 John J. Kingman Rd, Suite 0944 Ft Belvoir, VA 22060-6218	1 cy
AFRL/VSIL Kirtland AFB, NM 87117-5776	2 cys
AFRL/VSIH Kirtland AFB, NM 87117-5776	1 cy
Official Record Copy AFRL/DELC/Timothy Madden	5 cys